Communication

Intrinsic plasmon-phonon interactions in highly-doped graphene: A near-field imaging study

Francisco J Bezares, Adolfo De Sanctis, Jose R.M. Saavedra, Achim Woessner, Pablo Alonso-González, Iban Amenabar, Jianing Chen, Thomas Bointon, Siyuan Dai, Michael M. Fogler, D. N. Basov, Rainer Hillenbrand, Monica Felicia Craciun, F. Javier Garcia de Abajo, Saverio Russo, and Frank H.L. Koppens

Just Accepted

Intrinsic Plasmon-phonon Interactions in Highly-doped Graphene: A Near-field Imaging Study

Francisco J. Bezares,[†,@] Adolfo De Sanctis,[‡,@] José M. Saavedra,[†,@] Achim Woessner,[†] Pablo Alonso-González,[§,‖] Iban Amenabar,[§] Jianing Chen,[ℓ] Thomas H. Bointon,[‡] Siyuan Dai,[⊥] Michael M. Fogler,[⊥] Dimitri N. Basov,[⊥] Rainer Hillenbrand,[§,#] Monica F. Craciun,[‡] Javier García de Abajo,[†,¶,*] Saverio Russo[‡,*] and Frank H.L. Koppens[†,¶,*]

[†]ICFO-The Institute of Photonic Sciences, The Barcelona Institute of Science and Technology, 08860 Barcelona, Spain

[‡]Center for Graphene Science, College of Engineering Mathematical and Physical Sciences, University of Exeter, Exeter, UK

[§]CIC nanoGUNE Consolider, 20018 Donostia-San Sebastián, Spain

[‖]Departamento de Física, Universidad de Oviedo, 33007, Oviedo, Spain

[ℓ]Institute of Physics, Chinese Academy of Sciences, 100190, Beijing, China

[⊥]Department of Physics, University of California, San Diego, La Jolla, California 92093, USA

[#]IKERBASQUE, Basque Foundation for Science, 48011 Bilbao, Spain

[¶]ICREA-Institució Catalana de Recerca i Estudis Avançats, Passeig Lluís Companys 23, 08010 Barcelona, Spain

E-mail: javier.garciadeabajo@icfo.es;s.russo@exeter.ac.uk;frank.koppens@icfo.eu

---

[*]To whom correspondence should be addressed

Abstract

As a two-dimensional semi-metal, graphene offers clear advantages for plasmonic applications over conventional metals, such as stronger optical field confinement, *in situ* tunability and relatively low intrinsic losses. However, the operational frequencies at which plasmons can be excited in graphene are limited by the Fermi energy E_F, which in practice can be controlled electrostatically only up to a few tenths of an electronvolt. Higher Fermi energies open the door to novel plasmonic devices with unprecedented capabilities, particularly at mid-infrared and shorter-wave infrared frequencies. In addition, this grants us a better understanding of the interaction physics of intrinsic graphene phonons with graphene plasmons. Here, we present $FeCl_3$-intercalated graphene as a new plasmonic material with high stability under environmental conditions and carrier concentrations corresponding to $E_F > 1$ eV. Near-field imaging of this highly-doped form of graphene allows us to characterize plasmons, including their correspoding lifetimes, over a broad frequency range. For bilayer graphene, in contrast to the monolayer system, a phonon-induced dipole moment results in increased plasmon damping around the intrinsic phonon frequency. Strong coupling between intrinsic graphene phonons and plasmons is found, supported by *ab initio* calculations of the coupling strength, in good agreement with the experimental data.

KEYWORDS: *graphene plasmons, electron-phonon interactions, 2D intercalation, highly-doped graphene, s-SNOM*

Doped graphene is of fundamental importance for a plethora of applications, including graphene plasmonic device technology development.[1–7] Control over the doping level enables surface plasmons (SPs), whose wavelength scales with the fourth root of the Fermi Energy E_F. In addition, SPs interactions with the *zone-center*, in-plane optical phonons in graphene are intriguing as they are predicted to exhibit unconventional mixing of plasmon and phonon polarizations due to the 2-dimensional character of this material.[5] Although only Raman-active in single-layer graphene, the optical phonon becomes infrared (IR) active in bilayer graphene, *i.e.* it acquires a net dipole moment, due to broken inversion symmetry and

variation of the electron-phonon coupling under an electric field.[9] This makes it amenable

for many other advanced applications, such as phonon lasers[9] as well as non-linear optical,

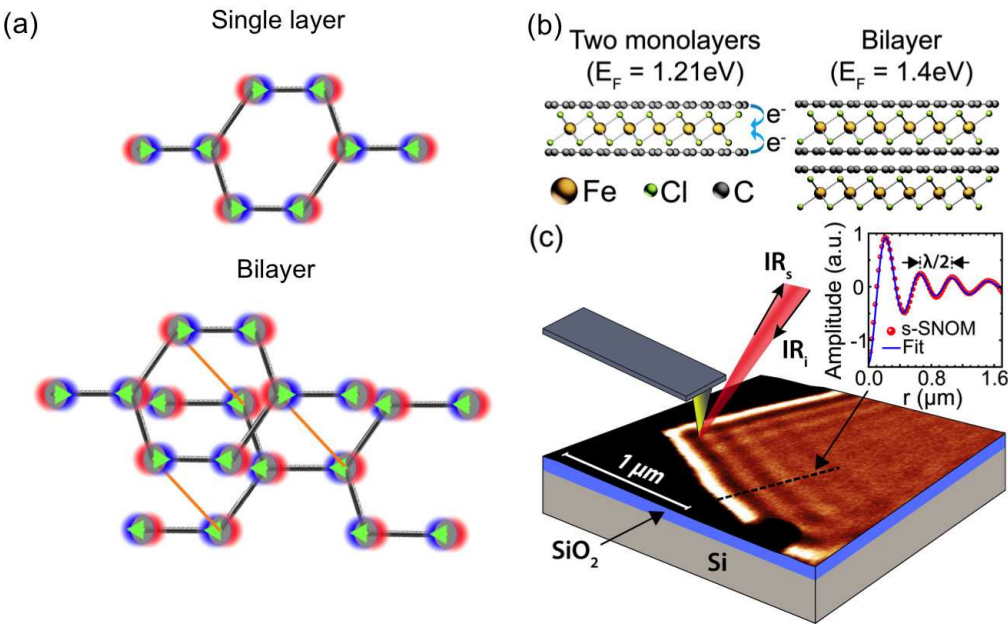quantum communication and slow-light devices.[10]

Figure 1: **Atomic structure and s-SNOM imaging. a** Atomic structure diagrams of monolayer (*top*) and bilayer (*bottom*) graphene showing the phonon-induced charge densities for vanishing *in-plane* wavevector (defined in text) in these structures. Inversion symmetry leads to a zero net dipole moment in the monolayer. In contrast, the lack of inversion symmetry makes the phonon mode IR-active in bilayer graphene. **b** Atomic layer structure diagram of $FeCl_3$-intercalated graphene. Monolayers of $FeCl_3$ form in between the graphene layers (*left*). The graphene layers are represented in gray color. A bilayer $FeCl_3$-intercalated graphene is formed when two carbon monolayers are present with no $FeCl_3$ molecules in between (*right*). **c** s-SNOM experimental setup diagram. SPs in graphene are excited via focusing of IR light onto a metalized AFM tip. Near-field images of SPs are obtained by scanning the sample spatially. Inset: s-SNOM line profile, extracted from 2D image (black dashed line), smoothened and corrected for geometrical decay ($1/\sqrt{r}$), where r represents the radial distance of propagation of AFM tip-induced traveling SPs. The plasmon wavelength is given by twice the measured fringe spacing. The red line is a fit to data (see Supplementary Information).

Recently, calculations by Low *et al.*[11] predicted novel plasmonic behavior in bilayer

graphene at higher carrier concentration levels and, in particular, giant plasmonic enhance-

ment of IR phonon absorption. Moreover, taking advantage of plasmon-phonon interactions

in bilayer nanoribbons, Yan *et al.*[12] experimentally demonstrated Fano-like phonon-induced transparency. However, many questions regarding the nature of interactions between surface plasmons and intrinsic phonons in graphene remain unexplored, such as the strength of the plasmon-phonon coupling and the effects of dipolar moment contributions to plasmon decay. For instance, optical phonons in monolayer graphene are regarded by many as a source of plasmon damping,[13] despite the lack of a net dipole moment of those phonons, which one would expect to result in reduced plasmon-phonon interaction.

In this letter, we study for the first time propagating plasmons in highly doped intercalated graphene. In particular, we use near-field plasmon imaging to study the effects of electron-phonon interactions on its plasmonic dispersion and damping. We show that the phonon-induced dipole in bilayer graphene is distinctly different from that in monolayer graphene and leads to hybridization of the plasmon mode at the phonon frequency in the former, as evidenced by anti-crossing behavior in the dispersion of the material. In monolayer graphene, inversion symmetry leads to a cancellation of the induced-charge contributions coming from each of the two atoms in the unit cell, thus resulting in a vanishing dipole moment within the unit cell for zero parallel (*in-plane*) wavevector. In contrast, the lack of inversion symmetry in bilayer graphene leads to a net phonon-induced dipole per unit cell, therefore enabling hybridisation between plasmonic and vibrational modes. This is depicted in the diagram in Fig. 1(a), where the atomic structure of monolayer (*top*) and bilayer graphene (*bottom*) is presented, together with the phonon-induced charge densities for each of the represented normal modes. In addition, we compare to first-principles calculations from which we obtain the value of the phonon-induced dipole moment per unit cell by means of *ab initio*, quantum chemistry methods. We show that experiment agrees well with theoretical results.

In order to investigate the effects of electron-phonon interactions, we performed plasmon

4

nanoimaging measurements in graphene at unprecented high intrinsic carrier concentrations (corresponding to $E_F > 1$ eV), achieved by intercalating graphene with $FeCl_3$.[14] This new material has been recently used in optoelectronic applications[15] and it showed an extraordinary linear dynamic range,[16] together with an unexpected resilience to environmental conditions.[17] To our knowledge, this is the first near-field observation of propagating plasmons with energies exceeding 0.2 eV.

We studied samples with two different types of intercalated graphene structures; 1) one in which $FeCl_3$ intercalates in between each graphene layer of a flake, which was previously a bilayer, to form two separated single layers and 2) one in which a bilayer flake remains free of $FeCl_3$ in between its layers after fabrication. A diagram of the atomic structure of these two cases can be seen in Fig. 1(b). The $FeCl_3$-intercalation resulted in carrier concentrations $n \geq 4.8$ x 10^{13} and 5.4 x 10^{13} cm^{-2}, for the two-monolayer and bilayer graphene samples, respectively. This corresponds to a Fermi energy E_F of 1.21 eV (~ 0.8eV for each of the two monolayers) on the two-monolayer sample, and 1.4 eV for the bilayer graphene. The high carrier densities result in an upshift of the G-bands in the Raman spectra of the samples, with respect to pristine graphene, as well as a variation in the shape of the 2D bands, as can be seen in Figs. S1 and S2 of the Supplementary Information, thus allowing for quantitative extraction of carrier concentrations from the careful analysis of the Raman features.[18,19] The carrier concentrations obtained using this method are also in excellent agreement with the plasmon dispersion measured on each corresponding sample.

scattering-Scanning Near-field Optical Microscopy (s-SNOM)[20,21] was used to image the near-field properties of highly-doped graphene with ~ 20 nm resolution, and at a broad frequency range. Fig. 1(c) presents a diagram of the experimental scheme where a tunable IR/MIR laser is focused onto the AFM tip of our s-SNOM setup in order to study the near-field on a $FeCl_3$-intercalated graphene sample. The graphene lies on a SiO_2/Si substrate.

The confined electromagnetic field at the AFM tip provides the momentum needed to excite propagating plasmons in the graphene. These plasmons can be reflected at the edge of the flake,[22,23] and subsequently interact with the tip. This results in a scattered optical field from the tip, which is detected in the far-field. As such, and as previously reported,[20,21,24] these type of measurements allow for the detection and real-space imaging of graphene plasmons, from which the SPs wavelength (*i.e.* momentum) can be measured, as shown in Fig. 1(c). All the measurements were performed at different instances over a period of time exceeding 18 months and under ambient conditions with no observable signs of sample degradation.

The plasmon dispersion is extracted from the above-mentioned near-field images by probing the plasmon wavelength (obtained by fitting oscillatory response) for a wide range of excitation frequencies. Fig. 2 shows the dispersion of the measured plasmons for the two-monolayer (*blue dots*) and bilayer system (*red dots*). The error bars are smaller than the size of the symbols. The dashed magenta curve represents the plasmon dispersion resulting from the simple expression for the *in-plane* wavevector $k_\parallel$, parallel to the graphene layer,

$$k_\parallel = (\epsilon_s + 1)\frac{i\omega}{4\pi\sigma}, \tag{1}$$

where σ is the 2D conductivity, ω is the frequency, and ϵ_s is the substrate permittivity. This corresponds to an uncoupled (*free-standing*) graphene monolayer. Due to strong coupling between the graphene plasmons and the SiO_2 *substrate phonons*, the plasmon dispersion is modified, which is captured by including the frequency dependence of the substrate permittivity $\epsilon_s(\omega)$. A comparison between the model and the experimental data shows clear evidence of splitting of the plasmon dispersion due to the hybridization of the plasmon mode with SiO_2 substrate surface phonons,[13,25,26] similar to previous reports on SPs in nanoribbons[27] and nanodots[8] on a SiO_2 substrate. In general, the data and model are in reasonable agreement when σ is substituted by a Drude conductivity with Fermi energy E_F=1.21 eV.

This confirms that the Drude weight of the plasmon is very high, thanks to the efficient intercalation process. In this study, plasmons were probed up to energies of ~0.28 eV (see Supplementary Information, Fig. S5). We remark that the interband region, indicated by the dashed green line, is "far" from the plasmon dispersion indicating the potential for this highly doped graphene to carry plasmons up to energies of 1 eV. Further studies are required to demonstate this, as it is very challenging to couple light with high energy graphene plasmons because the plasmon wavelength is very small (below 20 nm).
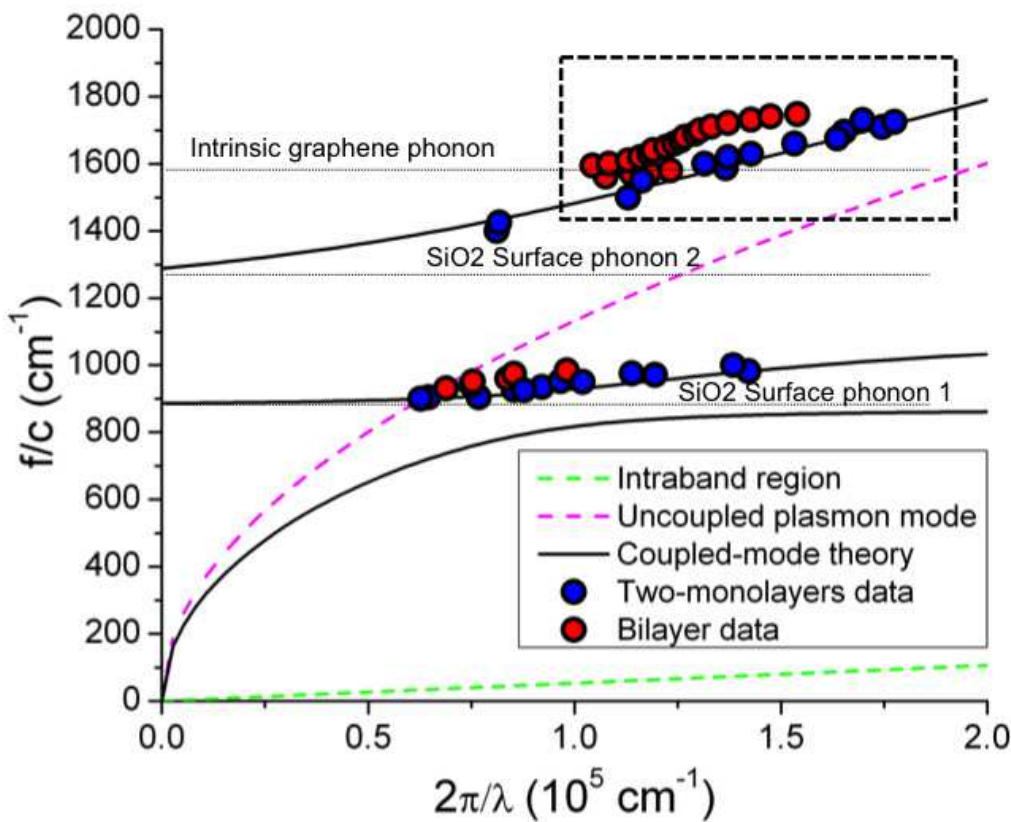

Figure 2: **Plasmon dispersion.** Blue and red symbols correspond to the experimentally measured dispersion of the two-monolayer $FeCl_3$-intercalated graphene and the bilayer sample, respectively. The dashed magenta curve represents the calculated dispersion of an uncoupled (*free-standing* graphene) plasmon with $E_F = 1.21\,eV$. The black curve corresponds to coupled-mode theory calculations for plasmons interacting with SiO_2 substrate surface phonons. The green dashed line delineates the intraband electronic transition region. Phonon frequencies of graphene and SiO_2 are indicated by horizontal dotted curves. The data within the dashed-squared region is analysed more in detail in the next figure.

While the dispersion of the bilayer graphene is expected to be shifted due to the higher effective Fermi energy in comparison to the two-monolayer system, it is also important to note the modal anti-crossing feature present in the bilayer graphene at the graphene phonon frequency of ~ 1585 cm^{-1}. This feature is not observed on the two-monolayer sample. This can be seen more clearly in Fig. 3, which displays s-SNOM 2D images of the two-monolayer (*top*) and bilayer (*bottom*) samples. The scanned areas shown for each sample are approximately the same. The images correspond to incident frequencies of 1590, 1586 and 1569 cm^{-1} for the two-monolayer sample and frequencies of 1600, 1585 and 1570 cm^{-1} for the bilayer sample (Additional s-SNOM images for a wider frequency range are shown in the Supplementary Information, Fig. S3.). For the two-monolayer sample, the plasmon interference fringes show a very similar pattern for the three frequencies, and exhibit a gradual decrease in spacing for increasing frequencies, as expected. The bilayer sample behaves distinctly different: as the incident frequency approaches to the phonon frequency, the visibility of the fringes[24] decreases and eventually almost no interference fringes are observed at ~ 1585 cm^{-1}. As the incident frequency further increases, away from the graphene phonon frequency, the fringes begin to gradually re-appear and their amplitude increases, showing prominent, muliple fringes in each image on both sides of the phonon frecuency (See also Fig. S3).

The left panels in Fig. 3 correspond to the dispersion data within the *dashed-squared* region in Fig. 2 for the two-monolayer (*top*) and bilayer (*bottom*) samples. The data highlights clear diferences between the dispersive behavior of the two samples. Here, anti-crossing behavior at the graphene *intrinsic* phonon frequency is clearly observed in the dispersion of the bilayer sample (*bottom*) whereas this feature is absent on the two-monolayer sample (*top*). The frequency interval between measurements around the graphene phonon frequency was no larger than 4 cm^{-1}, which is smaller than the energy width of the anti-crossing ($\Delta\omega \sim$ 37 cm^{-1}). This leads to a quantitative value for the electron-phonon coupling strength, in units of uncoupled frequency ω_0,[5] $\Delta\omega/\omega_0 \sim 2.3\%$. We attribute the splitting in the plasmon

dispersion of the bilayer graphene to the breaking of inversion symmetry in this system, causing a finite dipole moment and renders the graphene phonon mode IR-active.

The background color plots in Fig. 3 (left panels) correspond to the calculated imaginary part of the Fresnel reflection coefficient, which is a suitable magnitude to reveal the dispersion and strength of optical modes in graphene.[6] This is in turn obtained from the 2D conductivity, where we include contributions from intrinsic phonons in the latter, as obtained from *ab initio* calculations.[28] More precisely, an additional phonon term is incorporated, which is proportional to the squared dipole associated with the carbon phonon mode per unit cell. Our calculations reveal a net dipole in the bilayer structure, in contrast to a vanishing dipole in the monolayer for vertical optical transitions. This readily translates into the presence of a phonon-induced splitting of the plasmon mode in the carbon bilayer, which is absent in the two-monolayer sample. Good agreement between the experimental data and the calculated splitting is observed.

We now turn our attention to the impact of the plasmon-phonon coupling on plasmon lifetime. Given a plasmon wavevector with real and imaginary parts k_1 and k_2, respectively, depending on the different cases, the damping $\gamma = k_2/k_1$ of graphene SPs is typically determined by possible decay channels such as impurity and defect scattering, electron-hole pair creation as well electron-phonon scattering.[5,13] Although radiative and Landau damping can also play a role in some particular cases, their influence is expected to be neglegible in our experiments.[13] Here, we obtained the experimental value of γ for each incident frequency by fitting the line profile of s-SNOM 2D maps to an exponential function using the *least-square* fit method (see Supplementary Information, Fig. S4).

A comparison between the frequency dependence of the modal lifetime of the two samples is shown in Fig. 4. The data corresponding to the bilayer sample show a sharp lifetime
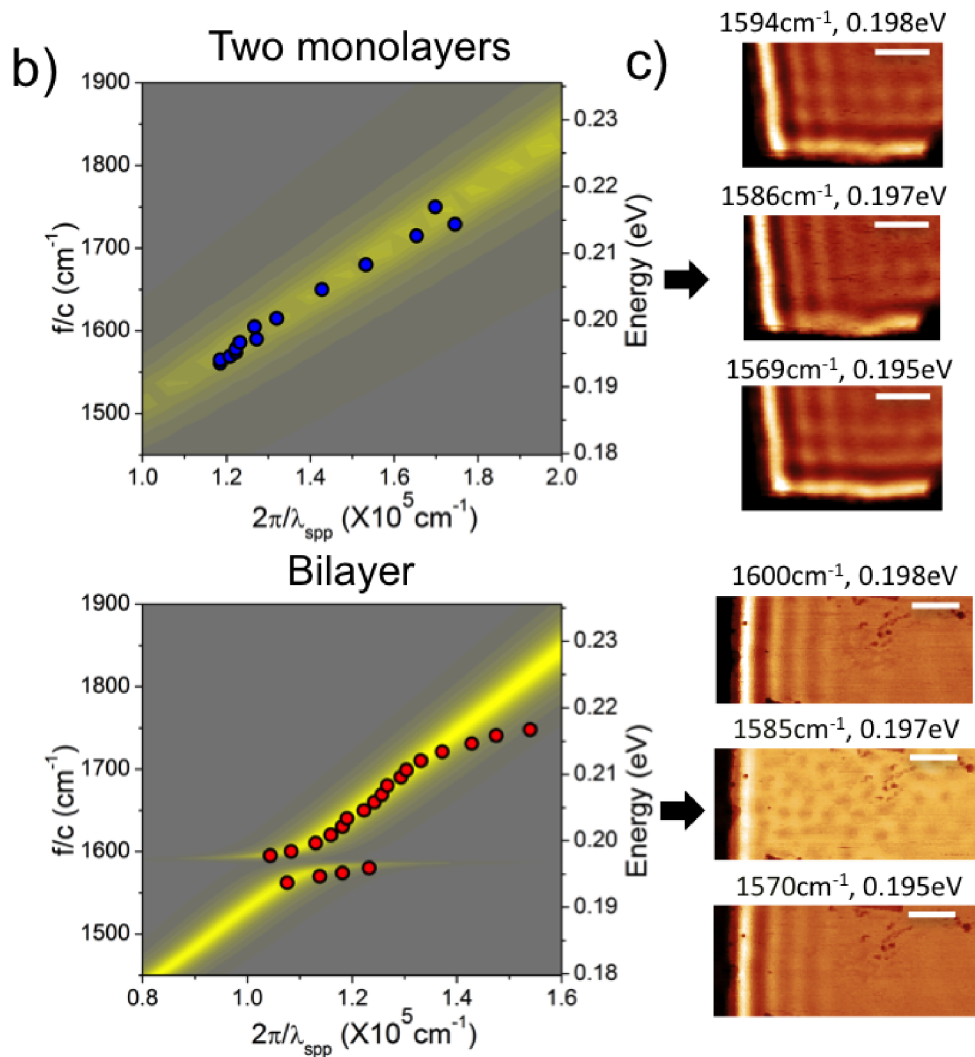
Figure 3: **Intrinsic plasmon-phonon coupling.** Left plots: Dispersion diagrams within the dashed-squared region in Fig. 2 for the two-monolayer (*top*) and bilayer (*bottom*) samples. The color background corresponds to the imaginary part of the Fresnel reflection coefficient for p-polarization. Coupling to IR-active phonons is apparent in bilayer graphene, whereas no coupling is observed in monolayer graphene. Right plots: s-SNOM images of the $FeCl_3$-intercalated flakes at different incident frequencies, as labeled. The images correspond to approximately the same area on each sample. Scale bar: ~ 500 nm.

1
2
3
4
5
6
7
8
9
10
11
12
13
14
15
16
17
18
19
20
21
22
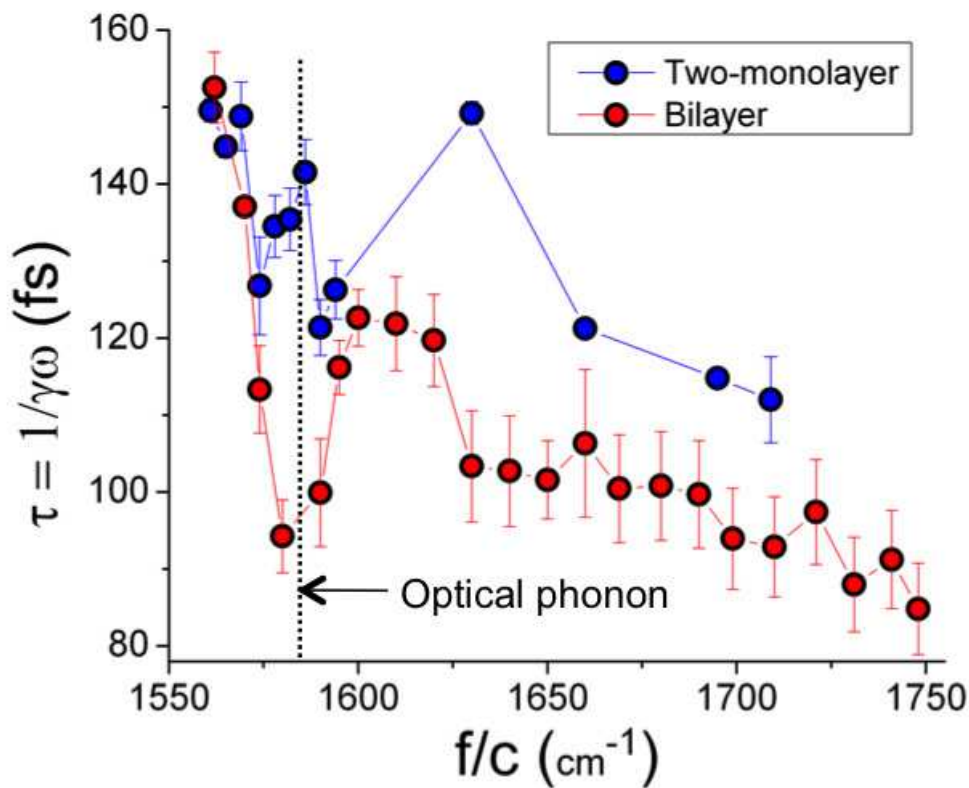23
24
25
26
27
28
29
30
31
32
33
34
35
36
37
38
39
40

Figure 4: **Mode lifetimes.** Measured lifetimes of modes in two-monolayer (blue symbols) and bilayer (red symbols) samples. The vertical dotted line marks the *intrinsic* graphene phonon frequency. A significant decrease in lifetime is observed in bilayer graphene at the phonon frequency, in contrast to the two-monolayer sample, where a slight increase is observed.

41
42
43
44
45
46
47
48
49
50
51
52
53
54
55
56
57
58
59
60

decrease at the phonon frequency. This is in stark contrast to the plasmon lifetime of the two monolayer sample at the same frequency. The lifetime of both samples experience a gradual decrease above the phonon frequency, possibly due to the opening of an additional decay channel beyond the phonon frequency, as reported by Yan *et al.*[13] However, at these frequencies, the lifetime of the two-monolayer sample is larger than the corresponding lifetime of the bilayer. It is important to note that, on one hand, the measured lifetime corresponds to a hybrid mode, which is plasmonic and phononic in character.[23,29,30] On the other hand, however, our definition of the lifetime does not take into account variations of the group velocity of the mode. Thus, although the plotted values in Fig. 4 under-estimate phononic contributions to the lifetime, our approach allows for a quantitative analysis of the lifetime near the graphene phonon resonance, particularly around the phonon frequency. The results also show that electronic damping of the measured mode is affected by electron-phonon interactions, particularly at the phonon frequency and also beyond. The data for the two-monolayer sample shows a marked increase in lifetime around a frequency of ~ 1631 cm^{-1}, however, the reasons for this behavior are unclear. Further studies on higher quality samples are required for a more detailed quantification of the role of intrinsic optical phonons on the plasmon lifetime.

In conclusion, we have observed propagating plasmons in ultra highly doped graphene with Fermi energy exceeding 1.2 eV and a splitting in the plasmon dispersion due to the interactions of plasmons with the finite dipolar moment of intrinsic optical phonons in bilayer graphene. This effect is not observed in two-monolayer graphene because in such case there is no effective phonon dipole moment due to inversion symmetry. We further present *ab initio* calculations in excellent quantitative agreement with the measured dispersion relations, confirming the existence of a net dipole associated with phonons in bilayer graphene, but not in monolayer graphene. Our results correlate with lifetime measurements and show that electron-phonon interactions play a substantial role in plasmonic decay, at and beyond the graphene *intrinsic* phonon frequency. These results are important for the development

of future graphene plasmonic devices, particularly as the excitation of graphene plasmons at energies of 0.2 eV, the optical phonon energy, and above may be amenable for novel applications such as photodetectors and sensors.

Acknowledgement

Authors Contributions

@ These authors contributed equally to this work.

Supporting Information Available

Detailes about Raman analysis of samples, additional relevant s-SNOM images, data fitting method and theoretical calculations.

This material is available free of charge via the Internet at `http://pubs.acs.org/`.

Competing Financial Interests

The authors declare no competing financial interest.

References

(1) Koppens, F. H. L.; Chang, D. E.; García de Abajo, F. J. *Nano Letters* **2011**, *11,* 3370-3377.

(2) Low, T.; Avouris, P. *ACS Nano* **2014**, *8,* 1086-1101.

(3) Hwang, E. H.; Sensarma, R.; Das Sarma, S. *Phys. Rev. B* **2010**, *82,* 195406.

(4) Grigorenko, A. N.; Polini, M; Novoselov, K. S. *Nature Photonics* **6**, *20112,* 749-758.

(5) Jablan, M.; Soljačić, M; Buljan, H. M. *Phys. Rev. B* **2011**, *83,* 161409(R).

(6) García de Abajo, F. J. *ACS Photonics* **2014**, *1,* 135-152.

(7) Basov, D. N.; Fogler, M. M; García de Abajo, F. J. *Science* **2014**, *354,* 195.

(8) Zhu, X.; Wang, W.; Yan, W.; Larsen, M. B.; Bøggild, P.; Pedersen, T. G.; Xiao, S.; Zi, J.; Mortensen, N. A. *Nano Letters* **2014** *14,* 2907-2913.

(9) Kuzmenko, A. B.; Benfatto, L.; Cappelluti, E.; Crassee, I.; van der Marel, D.; Blake, P.; Novoselov, K. S.; Geim, A. K. *Phys. Rev. Lett.* **2009** *103,* 116804.

(10) Tang, T-T.; Zhang, Y.; Park, C-H.; Geng, B.; Girit, C.; Hao, Z.; Martin, M. C.; Zettl, A.; Crommie, M. F.; Louie, S. G. *et al. Nature Nanotech.* **2009** *5,* 32-36.

(11) Low, T.; Guinea, F.; Yan, H.; Xia, F.; Avouris, P. *Phys. Rev. Lett.* **2014** *112,* 116801.

(12) Yan, H.; Low, T.; Guinea, F.; Xia, F.; Avouris, P. *Nano Letters* **2014** *14,* 4581-4586.

(13) Yan, H.; Low, T.; Zhu, W.; Wu, Y.; Freitag, M.; Li, X.; Guinea, F.; Avouris, P.; Xia, F. *Nature Photonics* **2013** *7,* 394-399.

(14) Khrapach, I.; Withers, F.; Bointon, T. H.; Polyushkin, D. K.; Barnes, W. L.; Russo, S.; Craciun, M F. *Adv. Mat.* **2012** *24,* 2844-2849.

(15) De Sanctis, A.; Barnes, M. D.; Amit, I.; Craciun, M. F.; Russo, S. *Nanotechnology* **2017** *28,* 124004.

(16) De Sanctis, A.; Jones, G. F.; Wehenkel, D.; Bezares, F.; Koppens, F. H. L.; Craciun, M. F.; Russo, S. *Science Advances* **2017** *3(5),* e1602617.

(17) Wehenkel, D. J.; Bointon, T. H.; Booth, T.; Bøggild, P.; Craciun, M. F.; Russo, S. *Sci. Rep.* **2015** *5,* 7609.

(18) Bointon, T. H.; Jones, G. F.; De Sanctis, A.; Hill-Pearce, R.; Craciun, M. F.; Russo, S. *Sci. Rep.* **2015** *5,* 16464.

(19) Zhan, D.; Sun, L.; Ni, Z.; Liu, L.; Fan, X.; Wang, Y.; Yu, T.; Lam, Y. M.; Huang, W.; Shen, Z. *Adv. Func. Mat.* **2010** *20,* 3504-3509.

(20) Chen, J.; Badioli M.; Alonso-Gonzalez, P.; Thongrattanasiri, S.; Huth, F.; Osmond, J.; Spasenovic, M.; Centeno, A.; Pesquera, A.; Godignon, P. *et al. Nature* **2012** *487,* 77-81.

(21) Fei, Z.; Rodin, A. S.; Andreev, G. O.; Bao, W.; McLeod, A. S.; Wagner, M.; Zhang, L. M.; Zhao, Z.; Thiemens, M.; Dominguez, G. *et al. Nature* **2012** *487,* 82-85.

(22) Gerber, J. A.; Berweger, S.; O'Callahan, B. T.; Raschke, M. B. *Phys. Rev. Lett.* **2014** *113,* 055502.
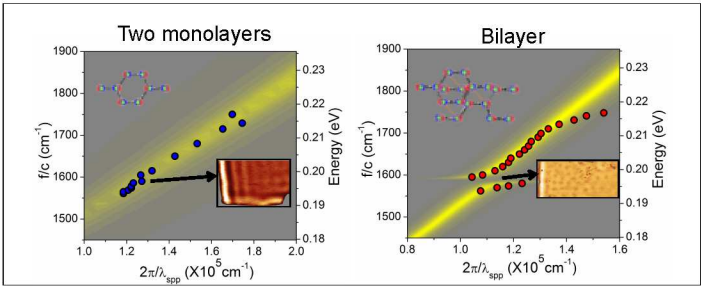
(23) Woessner, A.; Lundeberg, M. B.; Gao, Y.; Principi, A.; Alonso-Gonzalez, P.; Carrega, M.; Watanabe, K.; Taniguchi, T.; Vignale, G.; Polini, M. *et al. Nature Materials* **2015** *14,* 421-425.

(24) Schnell, M.; Carney, P. S.; Hillenbrand, R. *Nature Communications* **2013** *5,* 3499.

(25) Fei, Z.; Andreev, G. O.; Bao, W.; Zhang, L. M.; McLeod, A. S.; Wang, C.; Stewart, M. K.; Zhao, Z.; Dominguez, G.; Thiemens, M. *et al. Nano Letters* **2011** *11,* 4701-4705.

(26) Freitag, M.; Low, T.; Zhu, W.; Yan, H.; Xia, F.; Avouris, P. *Nature Communications* **2013** *4,* 1951.

(27) Brar, V. W.; Jang, M. S.; Sherrott, M.; Lopez, J. J.; Atwater, H. A. *Nano Letters* **2013** *13,* 2541-2547.

(28) Saavedra, J. R. M.; García de Abajo, F. J. *in preparation*

(29) Dai, S.; Ma, Q.; Liu, M. K.; Andersen, T.; Fei, Z.; Goldflam, M. D.; Wagner, M.; Watanabe, K.; Taniguchi, T.; Thiemens, M. *et al. Nature Nanotechnology* **2015** *10,* 682-686.

(30) Brar, V. W.; Jang, M. S.; Sherrott, M.; Kim, S.; Lopez, J. J.; Kim, L. B.; Choi, M.; Atwater, H. *Nano Letters* **2014** *14,* 3876-3880.

1
2
3
4
5
6
7
8
9
10
11
12
13
14
15
16
17
18
19
20
21
22
23
24
25
26
27
28
29
30
31
32
33
34
35
36
37
38
39
40
41
42
43
44
45
46
47
48
49
50
51
52
53
54
55
56
57
58
59
60

Graphical TOC Entry